Japanese Journal of Applied Physics **54**, 04DC05 (2015) **REGULAR PAPER**
http://dx.doi.org/10.7567/JJAP.54.04DC05

Impurity doping effects on impurity band structure modulation in two-dimensional n^+ and p^+ Si layers for future CMOS devices

Tomohisa Mizuno[1*], Yoshiki Nagamine[1], Yuhya Suzuki[1], Yuhta Nakahara[1], Yuhsuke Nagata[1], Takashi Aoki[1], and Toshiyuki Sameshima[2]

[1]*Department of Science, Kanagawa University, Hiratsuka, Kanagawa 259-1293, Japan*
[2]*Department of Engineering, Tokyo University of Agriculture and Technology, Koganei, Tokyo 184-8588, Japan*
E-mail: mizuno@info.kanagawa-u.ac.jp

Received September 7, 2014; revised October 25, 2014; accepted November 4, 2014; published online January 23, 2015

We experimentally studied the effects of n^+ and p^+ dopant atoms on the band structure modulation in two-dimensional (2D) Si layers for a wide range of dopant density N by the photoluminescence (PL) method. The bandgap E_G of both n^+ and p^+ 2D-Si strongly depends on N, and decreases with increasing N, which is attributable to the E_G narrowing effects δE_G even in 2D-Si. However, δE_G in the doped 2D-Si is much smaller than that in 3D-Si and depends on whether the dopant is donor or acceptor. We introduce a simple model for the small δE_G, considering the impurity band structure modulation in heavily doped 2D-Si. As a result, we can estimate source/drain dopant density dependence of a built-in potential of pn junction in a 2D-Si layer for CMOS devices. © 2015 The Japan Society of Applied Physics

1. Introduction

In two-dimensional (2D) Si layers, which are key structures for realizing future CMOS devices, such as extremely thin silicon-on-insulator (ETSOIs) and fin-type FET (FinFET) CMOS,[1,2] as well as Si photonic devices,[3,4] we experimentally demonstrated strong quantum confinement effects (QCEs).[5–8] Raman spectroscopy showed the asymmetrical broadening and peak downshift of Raman spectra in both (100) and (110) surface 2D-Si owing to phonon confinement effects (PCE) caused by Heisenberg's uncertainty principle of the phonon wave vector in a finite Si thickness T_S.[9–15] Moreover, bandgap (E_G) expansion due to 2D electron confinement effects was successfully measured by the photoluminescence (PL) method.[5–8] Both the QCEs of 2D electrons[16–18] and PCEs[19] cause a reduction in electron mobility. Furthermore, the QCEs modulate the energy-band structures of 2D-Si[20–22] and change the Si crystals from indirect-bandgap three-dimensional (3D) Si to a direct-bandgap material.[4,19,20,23]

Since pn junctions are key structures for realizing future CMOS devices, the study on QCEs in heavily doped 2D-Si is also of great importance. In our previous study,[7] the PL measurement showed that the E_G narrowing effect δE_G is reduced in the case of n^+ 2D-Si with a dopant of less than $4 \times 10^{20}\,\mathrm{cm}^{-3}$,[7] compared with that of n^+ 3D-Si.[24] This is attributable to both the impurity band of donors and conduction band tailing.[25] As a result, the built-in potential V_{BI} of the pn junction in the 2D-Si is expected to increase with increasing the n^+ dopant density.[7] Moreover, the ionization energy of donor atoms in doped one-dimensional (1D) Si has also been reported to increase with increasing the n^+ dopant density.[26] Therefore, to design the pn junction of CMOS devices composed of 2D-Si in detail and to estimate V_{BI}, it is very important to study both the reduced δE_G effect in detail and also the physical mechanism in both n^+ and p^+ 2D-Si for a wide range of dopant density N.

In this work, we experimentally studied the effects of n^+ and p^+ dopant atom on the band structures in heavily doped 2D-Si layers which are fabricated by oxidation-induced Si thinning after ion implantation into (100)-surface SOI substrates.[27] By the PL method, we confirmed that E_G strongly depends on the impurity dopant density N and rapidly decreases with increasing N in both n^+ and p^+ 2D-Si layers. However, δE_G in the heavily doped 2D-Si is much smaller than that in the doped 3D-Si. In addition, δE_G in n^+ 2D-Si is much smaller than that in p^+ 2D-Si. The reduced δE_G in doped 2D-Si may be attributable to the impurity band E_I modulation (IBM) effects in doped 2D-Si.

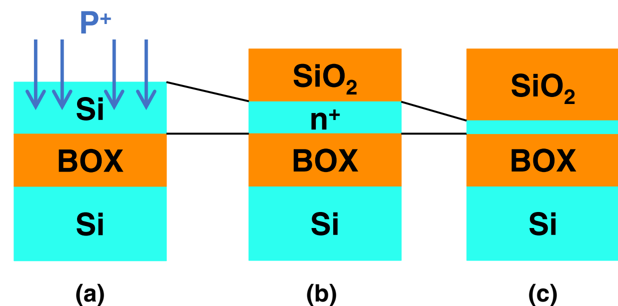

Fig. 1. (Color online) Schematic two-step oxidation fabrication steps for n^+ 2D-Si layers on the buried oxide layer. (a) After P^+ implantation into (100) bonded SOI substrates, (b) Si was thinned to about several nm by high-T oxidation at 1000 °C. (c) Additional low-T oxidation at 900 °C after (b) was carried out to form a sub-1-nm-thick Si layer.

2. Experimental procedure

To control the 2D-Si thickness T_S well, heavily doped n^+ and p^+ 2D-Si layers were fabricated by a two-step thermal oxidation induced thinning of (100)-surface bonded SOI wafer[28] with T_S of 55 nm and a buried oxide (BOX) thickness of 145 nm. The two-step thermal oxidation steps were low-temperature (T) (900 °C) oxidation after high-T oxidation (1000 °C) of donor P^+ or acceptor B^+ ion implanted SOI substrates. During the oxidation of SOI substrates, the P^+ and B^+ segregation coefficients m at the Si/SiO_2 interface are about 10 and 0.1, respectively.[29] As a result, after the oxidation of the SOIs, the P^+ density of the 2D-Si layers increases, but the B^+ density rapidly decreases.[7] Thus, it is necessary that P^+ donor and B^+ acceptor ions are implanted at different process steps to form heavily doped n^+ and p^+ layers, as shown in Figs. 1 and 2.

 © 2015 The Japan Society of Applied Physics

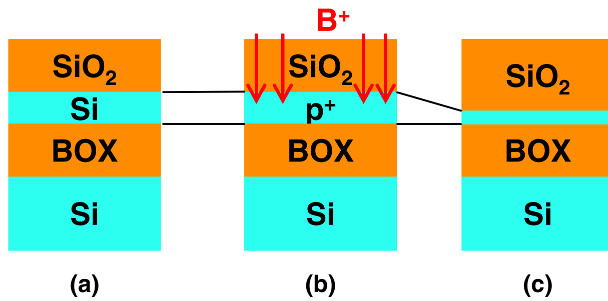

Fig. 2. (Color online) Schematic two-step oxidation fabrication steps for p^+ 2D-Si layers. (a) After a high-T oxidation process at 1000 °C to form about 10-nm-thick Si layers, (b) B^+ was implanted into thinned (100) SOI. (c) Additional low-T oxidation at 900 °C after (b) was carried out to form a sub-1-nm-thick-Si layer.

Figures 1 and 2 show the fabrication steps for n^+ and p^+ 2D-Si layers, respectively. In the case of n^+ 2D-Si, after P^+ implantation at ion energy $E_I = 15$ keV with various ion doses, D_I from 1.5×10^{13} to 2×10^{14} cm^{-3} into (100) SOI as shown in Fig. 1(a), Fig. 1(b) shows that a 55-nm-thick Si layer was thinned to about 5 nm of T_S by high-T oxidation (1000 °C). As shown in Fig. 1(c), additional low-T oxidation (900 °C) was carried out to form an n^+ 2D-Si layer with T_S of less than 1 nm. As a result, phosphorus atoms are condensed in the 2D-Si. To reduce the segregation effects of the boron in the case of the p^+ 2D-Si thinning, after the initial high-T oxidation process (1000 °C) to form about 10-nm-thick Si layers, as shown in Fig. 2(a), Fig. 2(b) shows the ion implantation of B^+ at $E_I = 27$ keV with various D_I from 3×10^{15} to 1×10^{16} cm^{-3} into about 10-nm-thick (100) SOI. As shown in Fig. 2(c), additional low-T oxidation (900 °C) was carried out to form a p^+ 2D-Si layer without a large reduction of boron density. P^+ and B^+ ion implantation conditions were determined by a process simulator.[30] As a result, the maximum impurity densities of phosphorus and boron that can be achieved were formed to be about 2.1×10^{21} and 4.0×10^{19} cm^{-3} at T_S of 0.5 nm, respectively.

Figures 3(a) and 3(b) show high-resolution transmission electron microscopy (HRTEM) images of the cross section of a 0.5-nm-thick n^+ Si unit cell layer. Even in the heavily doped 2D-Si with the dopant density of 4×10^{20} cm^{-3}, Figs. 3(a) and 3(b) clearly show very uniform 2D-Si layer of good crystal quality seen as a good lattice image. T_S of the n^+ 2D-Si layer was 0.54 nm which is equal to the Si unit cell layer thickness. These images are similar to the HRTEM images of intrinsic 2D-Si.[5] T_S was also confirmed by a UV/visual reflection method[5] and was almost the same value obtained from the HRTEM images of Fig. 3. Thus, we successfully fabricated both n^+ and p^+ 2D-Si layers with T_S of a Si unit cell in this work.

Figure 4 shows the profile of the secondary ion mass spectrometry (SIMS) (solid line) and process simulation (dotted line) results for boron concentration N_B of the p^+ 2D-Si, where $D_I = 1 \times 10^{16}$ cm^{-2} and $T_S \approx 4$ nm, which is the minimum thickness for the SIMS detection limit. Here, the SIMS profile at the oxide/Si interface is inaccurate because of the SIMS detection limit. The average SIMS boron density $\overline{N_B} = \int_0^{T_S} N_B(x)\,dx/T_S \equiv 1.8 \times 10^{20}$ cm^{-3} in the Si layer (dashed line) is almost the same as that of the 2D simulation result (dotted line) of 1.2×10^{20} cm^{-3}.[30] Thus, in this study,

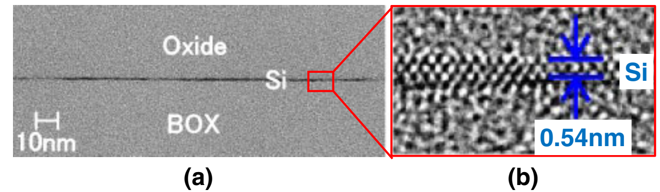

Fig. 3. (Color online) HRTEM images of the cross section of (100)-surface n^+ 2D-layer with $N_D = 4 \times 10^{20}$ cm^{-3} and $T_{OX} = 116$ nm. (a) Wide-area image showing a uniform and continuous n^+ 2D-Si layer, and (b) HRTEM images showing a good Si lattice and $T_S \approx 0.54$ nm, which equals T_S for the Si unit cell.

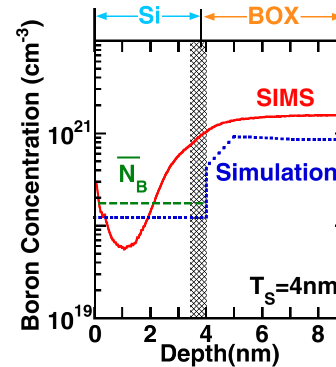

Fig. 4. (Color online) SIMS depth profile (solid line) and process simulation result (dotted line) for boron atoms after process in Fig. 2, where the boron dose is 1×10^{16} cm^{-2} and $T_S \approx 4$ nm. The dashed line shows the experimental average boron density (1.8×10^{20} cm^{-3}) in the Si layer which is obtained from the SIMS data, and is almost the same as the simulation result (1.2×10^{20} cm^{-3}). SIMS results at the SiO_2/Si interface are inaccurate because of the SIMS detection limit.

the N value of 2D-Si under various ion implantation conditions can be obtained from the process simulation results, and thus, the N value accuracy is on the order of 10%.

To study the crystal quality of the high-dose boron-ion-implanted Si layers, we carried out UV-Raman spectroscopy for thick p^+ Si layers without PCEs of asymmetrical Raman broadening in the lower wave number region,[7] where $T_S \approx 6.5$ nm and the Raman laser wavelength is 325 nm. Figure 5 shows the Raman spectra of p^+ Si layers with boron doses of 1×10^{16} cm^{-2} (solid line) and 3×10^{15} cm^{-2} (dotted line). Even at high boron doses, we observed no Raman peak from poly-Si at approximately 480 cm^{-1}, which shows that Si layers were not polycystallized by implantation with a high dose of boron ions. Moreover, the FWHM of high-dose p^+ Si, which is an indicator for the Si crystal quality, is only about 1.4 times as large as that of low dose p^+, n^+, and intrinsic Si layers, and thus the degradation in FWHM of high-dose p^+ Si is not so large. Therefore, ion implantation with high-dose p^+ probably induces a small reduction of the PL intensity, but the influence on E_G modulation is not so large.

In this work, we analyzed the E_G properties of n^+ and p^+ 2D-Si evaluated by PL method with 2.33 eV excitation laser at room temperature, where the PL intensity can be detected in (100)-surface 2D-Si with less than 1 nm.[6–8] Laser power P_L was set to be 1 mW to compress the P_L heating of Si,[6] and the laser diameter was 1 μm.

© 2015 The Japan Society of Applied Physics

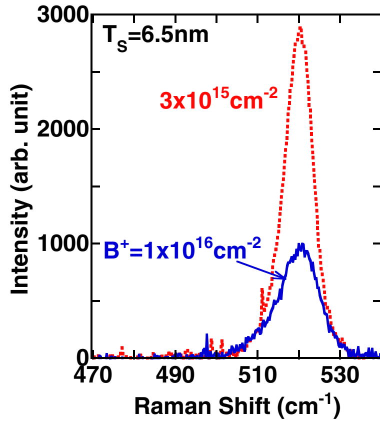

Fig. 5. (Color online) Raman spectra of p^+ layers with boron doses of $1 \times 10^{16}\,cm^{-2}$ (solid line) and $3 \times 10^{15}\,cm^{-2}$ (dotted line), where $T_S \approx$ 6.5 nm. There is no Raman peak from poly-Si at approximately $480\,cm^{-1}$, and the FWHM of high-dose p^+ Si is only about 1.4 times as large as that of low dose p^+ Si.

3. Results and discussion

3.1 Dopant density dependence of δE_G

In this section, we discuss E_G as a function of the dopant density in the doped 2D-Si by the PL measurement.

Figures 6(a) and 6(b) show the N dependence of the PL spectra of n^+ and p^+ 2D-Si, respectively, where $T_S = 0.5$ nm. The PL intensity I_{PL} and E_G, defined by the PL photon peak energy in both n^+ and p^+ 2D-Si, decrease with increasing N. The FWHM of the PL spectra also increases with increasing N.

The N dependence of I_{PL} in n^+ 2D-Si is replotted in Fig. 7. Here, the N error bars show the N accuracy of 10% order obtained by the data in Fig. 4 in this study. The experimental data can be empirically fitted by the following function of N:

$$I_{PL} \propto \exp\left(-\frac{N}{1.6 \times 10^{21}}\right), \tag{1}$$

where the correlation coefficient is about 0.98. I_{PL} rapidly decreases with increasing N, which is similar to that in 1D-Si,[31] and may be attributable to the reduction in the PL emission efficiency of the heavily doped 2D-Si with relatively poor crystalline quality compared with that of intrinsic 2D-Si.

The N dependences of E_G in n^+ and p^+ 2D-Si are also shown in Figs. 8(a) and 8(b), respectively. The E_G error bars show the PL resolution in this study. E_G in both n^+ and p^+ 2D-Si strongly depends on N and decreases markedly with increasing N. Figures 8(a) and 8(b) show that the experimental data can be empirically fitted by the following equation of N (dashed and dotted lines):

$$E_G(N) = E_0 + E_1 \exp\left(-\frac{N}{N_0}\right), \tag{2}$$

where the correlation coefficients of n^+ and p^+ 2D-Si are about 0.99 and 1, respectively. In the case of n^+ 2D-Si shown in Fig. 8(a), the parameters in Eq. (2) are shown in Eq. (3).

$$E_0 = 1.67\,\text{eV};\ E_1 = 62.0\,\text{meV};\ N_0 = 5.08 \times 10^{20}\,\text{cm}^{-3}. \tag{3}$$

On the other hand, in the case of p^+ 2D-Si shown in Fig. 8(b),

$$E_0 = 1.68\,\text{eV};\ E_1 = 53.4\,\text{meV};\ N_0 = 1.09 \times 10^{19}\,\text{cm}^{-3}. \tag{4}$$

Equations (3) and (4) show that E_0 and E_1 are almost independent whether the dopant is donor or acceptor. Here, Fig. 8(c) shows the N dependence of E_G in n^+ (circles) and p^+ (triangles) 2D-Si for a wide range of N, where the dashed

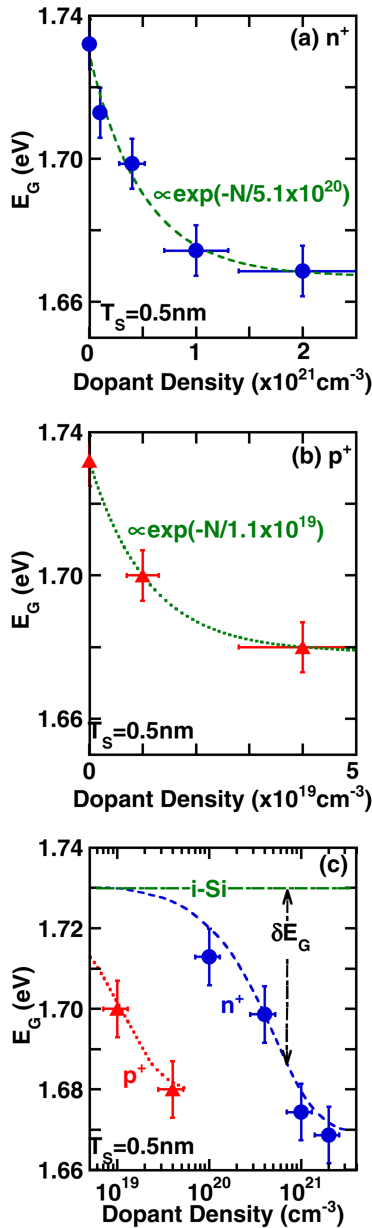

Fig. 8. (Color online) Experimental E_G vs simulated impurity density of (a) n^+ (circles), (b) p^+ 2D-Si (triangles), and (c) both n^+ and p^+ 2D-Si, where $T_S = 0.5$ nm. The dot-dashed line in (c) shows the E_G of i-Si. Vertical and lateral error bars show the PL resolution and N accuracy (Fig. 4 data) in this study, respectively. Dashed and dotted lines show the experimental fitting curves of $E_G = E_0 + E_1 \exp(-N/N_0)$ of Eq. (2) for n^+ and p^+ 2D-Si, respectively, where the correlation coefficient of n^+ 2D-Si is 0.99. E_0, E_1, and N_0 are shown in Eqs. (3) and (4). (c) shows that the N dependence of p^+ 2D-Si is considerably different from that of n^+ 2D-Si. δE_G shows the bandgap narrowing in doped Si compared with E_G of i-Si.

and dotted lines show Eq. (2) of n^+ and p^+ 2D-Si, respectively. The N dependence in p^+ 2D-Si is very different from that of n^+ 2D-Si, and thus, the N dependence in n^+ 2D-Si is much lower than that in p^+ 2D-Si. However, it is not clear whether the E_G of p^+ 2D-Si is saturated within $1 \times 10^{20}\,\mathrm{cm}^{-3}$ or not, because it is very difficult to realize a p^+ density of higher than $1 \times 10^{20}\,\mathrm{cm}^{-3}$. Equations (3) and (4) show that N_0 of n^+ 2D-Si is about 50 times as large as that of p^+ 2D-Si. This reduced E_G in both n^+ and p^+ 2D-Si is attributable to the bandgap narrowing effect δE_G (arrow) in the heavily doped Si,[24] which is caused by the impurity band

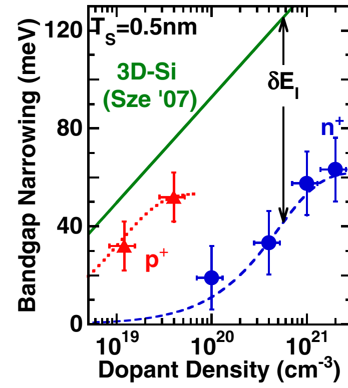

Fig. 9. (Color online) Experimental bandgap narrowing vs simulated impurity density of n^+ (circles) and p^+ 2D-Si (triangles), where $T_S = 0.5$ nm. The solid line indicates the empirical formula of 3D-Si.[24] Dashed and dotted lines indicate the calculated results of Eq. (5) for n^+ and p^+ 2D-Si, respectively. δE_I defined by Eq. (6) shows E_I modulation in doped 2D-Si. δE_G of doped 2D-Si also increases with increasing N, but is much lower than that of doped 3D-Si.

E_I including the conduction/valence band tailing in degenerate Si.[25,26]

Here, the N dependence of δE_G is defined by $\delta E_G(N) \equiv E_G(0) - E_G(N)$, where $E_G(0)$ is E_G of intrinsic 2D-Si. Figure 9 shows the experimental δE_G as a function of N in n^+ (circles) and p^+ (triangles) 2D-Si and the calculated δE_G of 3D-Si (solid line) given by δE_G (meV) $= 18.7 \ln(N/7 \times 10^{17})$.[24] δE_G of n^+ 2D-Si is much smaller than that of 3D-Si, but the difference in δE_G between p^+ 2D-Si and 3D-Si is very small. According to Eqs. (2)–(4), the δE_G of 2D-Si can be given by Eq. (5) and is shown as the dashed and dotted lines in Fig. 9:

$$\delta E_G(N) \equiv E_G(0) - E_G(N) = E_I\left(1 - \exp\left(-\frac{N}{N_0}\right)\right). \quad (5)$$

Large difference in δE_G between n^+ 2D-Si and 3D-Si may be attributable to the impurity band E_I modulation δE_I (arrow in Fig. 9) near the conduction band in the n^+ 2D-Si, as discussed in the next subsection. Thus, small difference in δE_G between p^+ 2D-Si and 3D-Si is considered to be due to the small E_I modulation near the valence band in the p^+ 2D-Si. Consequently, the reduced δE_G is characteristic of doped 2D-Si, but δE_G depends on whether the dopant is donor or acceptor.

3.2 Impurity band modulation of doped 2D-Si

To explain the difference in δE_G between 2D and 3D doped Si, as shown in Fig. 9, we consider that two physical mechanisms may exist. One is the reduced donor density caused by the deactivation effects of phosphorus atoms in the 2D-Si, and the other is impurity band modulation (IBM). According to the deactivation effect model, to explain the data in Fig. 9, the phosphorus activation rate in the 2D-Si should be reduced by about two orders of magnitude compared with that of 3D-Si. However, even in 1D-Si, the phosphorus activation rate caused by the enlarged ionization energy of phosphorus[32] is lower by only one order of magnitude than that of 3D-Si.[26] Thus, the possibility of the larger deactivation model is very low, and hence, we introduce the IBM model for explaining the small δE_G in this study.

 © 2015 The Japan Society of Applied Physics

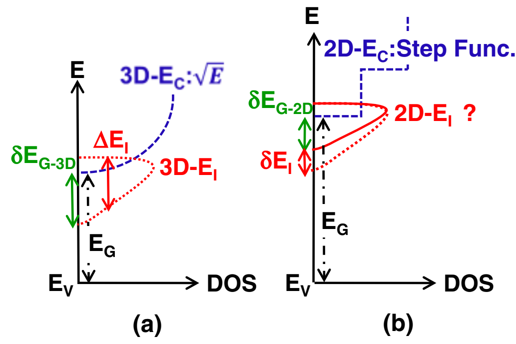

Fig. 10. (Color online) Schematic DOS functions (E vs DOS) for (a) n^+ 3D-Si[25] and (b) n^+ 2D-Si.[24] The DOS in 3D-Si is proportional to $\sqrt{E}$, but the DOS in 2D-Si shows a step function of E. Dashed and dotted lines show the conduction and impurity bands in doped Si, respectively. The solid line in (b) shows the modulated impurity band of n^+ 2D-Si. δE_G, ΔE_I, and δE_I are the E_G narrowing, E_I band-width, and E_I modulation, respectively.

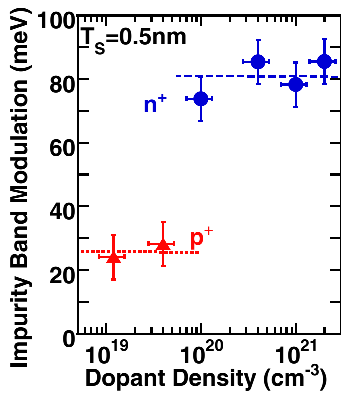

Fig. 11. (Color online) Experimental δE_I of n^+ (circles), δE_{IN}, and p^+ 2D-Si (triangles), δE_{IP}, as a function of simulated dopant density, where $T_S = 0.5$ nm. Both δE_{IN} and δE_{IP} are independent of dopant density, but the average δE_{IN} (81 meV) is about three times as large as the average δE_{IP} (26 meV).

Figures 10(a) and 10(b) show the schematic density of states (DOS) functions versus electron energy E near the conduction band in n^+ 3D-[25] and 2D-Si, respectively. In the case of n^+ 3D-Si, Fig. 10(a) shows that DOS(E) $\propto \sqrt{E}$,[24] and E_I, including the conduction band tailing, causes the δE_G.[25] Moreover, the bandwidth of E_I, ΔE_I, expands with increasing donor concentration N_D,[33] resulting in the increase in δE_G. On the other hand, Fig. 10(b) shows that the DOS of 2D-Si has a step function of E, which is due to the quantum confinement effects of electrons,[24] and thus, the E_G of 2D-Si increases. To explain the small δE_G in n^+ 2D-Si shown in Fig. 9, Fig. 10(b) shows that ΔE_I of n^+ 2D-Si may become narrower by δE_I which is attributable to IBM in 2D-Si, resulting in the reduced δE_G in the doped 2D-Si. Since E_G of doped Si; E_{GD}, is given by $E_{GD} = E_C - E_V - \delta E_G$, δE_G of doped 2D-Si, $\delta E_{G\text{-}2D}$, is reduced by the IBM of δE_I, compared with that of 3D-Si, $\delta E_{G\text{-}3D}$. Thus, δE_I can be expressed by

$$\delta E_I = \delta E_{G\text{-}3D} - \delta E_{G\text{-}2D}. \qquad (6)$$

From Eq. (6) and the data in Fig. 9, δE_I can be estimated in both n^+ (circles) and p^+ (triangles) 2D-Si layers, and is shown in Fig. 11. It is clear that δE_I is independent of N, and the average δE_I of n^+ and p^+ 2D-Si are about 81 and 26 meV, respectively. Therefore, δE_I of n^+ 2D-Si is about three times as large as that of p^+ 2D-Si. This suggests that δE_I strongly depends on whether the impurity is donor or acceptor, and the IBM of acceptors is very small. However, the physical mechanisms for both δE_I caused by the reduction of both the ΔE_I and conduction band tailing, and the difference in δE_I between the donor and acceptor are not currently understood. In contrast, the donor's ionization energy E_D increases in the case of 1D-Si,[32] and thus the large E_D ought to lead to a larger δE_G of doped 1D-Si. This tendency of a larger δE_G of 1D-Si is opposite to the experimental data showing a smaller δE_G of 2D-Si in this work.

3.3 Built-in potential of the pn junction in 2D-CMOS devices

According to the above discussion regarding band structure modulations in the doped 2D-Si, we analyzed the built-in potential of the pn junction V_{BI} in 2D-CMOS devices, and showed the difference in V_{BI} between n- and p-MOS.

Figure 12(a) shows a schematic cross section of ETSOIs with an optimized pn junction structure whose junction edge exists in the 2D-Si layer.[7] V_{BI} in a 2D-CMOS can be simply obtained[7] by considering δE_G in the doped 2D-Si, δE_{G2}, shown as the E_G distribution in Fig. 12(a) and Eq. (5). That is,

$$V_{BI}(N) \equiv \frac{E_{G2} + \delta E_{G2}}{2q} = \frac{E_{G2} + E_I(1 - \exp(N/N_0))}{2q}, \qquad (7)$$

where E_{G2} is E_G of the intrinsic 2D-Si of the channel, and q is the elementary charge. On the other hand, V_{BI} in a 3D-CMOS can be given by[24]

$$V_{BI}(N) \equiv \frac{E_{G3} + \delta E_{G3}}{2q} = \frac{E_{G3} + 18.7 \ln(N/7 \times 10^{17})}{2q}, \qquad (8)$$

where E_{G3} and δE_{G3} are E_G of the intrinsic 3D-Si of the channel and δE_G of doped 3D-Si, respectively. In addition, E_{G2} actually depends on the tensile strain ε in 2D-Si stressed by the thermal expansion mismatch between the surface oxide and 2D-Si layers.[34] For example, E_{G2} at $\varepsilon = 0\%$ is estimated to be 2.02 eV at $T_S = 0.5$ nm,[34] whereas E_{G2} at $\varepsilon = 0.34\%$ in this study was 1.73 eV, as shown in Fig. 8. Figures 12(b) and 12(c) show the dopant density dependence of V_{BI} of n- (solid line), p-MOS (dashed line), and 3D-Si (dotted line) at $\varepsilon = 0.34\%$ and $\varepsilon = 0\%$, respectively, obtained from Eqs. (7) and (8), where $T_S = 0.5$ nm. V_{BI} in the 2D-Si increases with increasing N because of the larger δE_{G2} for higher N. Moreover, V_{BI} at $\varepsilon = 0\%$ in both the n- and p-MOS is higher than 1 V for a wide range of N. However, V_{BI} of the n-MOS can be lower than that of the p-MOS in $N < 1 \times 10^{21}$ cm^{-3}. In addition, V_{BI} in the 2D-Si is much higher than that in 3D-Si by about 0.5 V, which is a characteristic of 2D-Si. The larger V_{BI} in 2D-Si becomes a physical limitation for realizing the normal operation of 2D-CMOS devices at lower supply voltage of less than 1 V.

4. Conclusions

We experimentally studied the effects of dopant atoms on the band structure modulation in n^+ and p^+ 2D-Si layers for a wide range of dopant density N by the PL method.

The PL intensity and bandgap E_G of both n^+ and p^+ 2D-Si strongly depend on N, and E_G rapidly decreases with increasing N, which is attributable to the E_G narrowing effect δE_G in the doped 2D-Si. Moreover, the δE_G in the doped 2D-

 © 2015 The Japan Society of Applied Physics

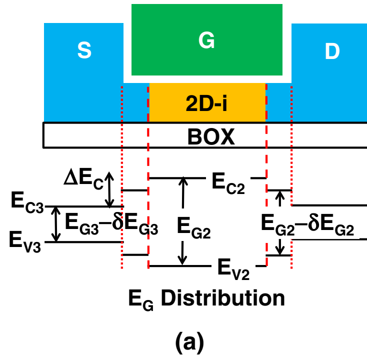

(a)

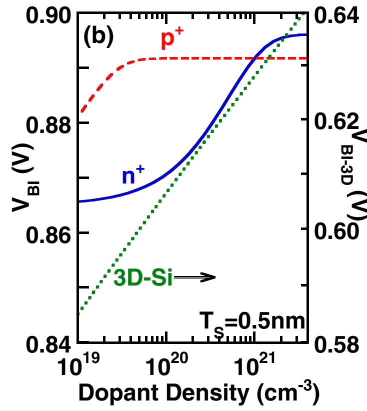

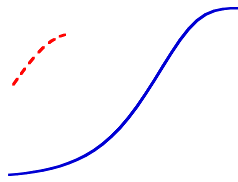

Si can be given by an exponential function of N. However, δE_G in the doped 2D-Si is much smaller than that of 3D-Si, and in particular, the δE_G in the n^+ 2D-Si is much smaller than that in the p^+ 2D-Si. We introduce a simple model for explaining the small δE_G in the n^+ 2D-Si, considering the phosphorus impurity band modulation δE_I including the conduction band tailing, which leads to a small δE_G in the doped 2D-Si. Moreover, we can experimentally demonstrate that the δE_I in the n^+ 2D-Si (81 meV) is about three times as large as that in the p^+ 2D-Si (26 meV), whose physical mechanism is not currently understood. Using the above E_G modulation in the n^+ and p^+ 2D-Si, we can analyze the pn junction properties in 2D-CMOS devices.

Consequently, according to the detailed E_G properties of the doped 2D-Si, we can precisely design a pn junction structure for future CMOS devices composed of 2D-Si structures.

Acknowledgements

We would like to thank Professor J. Nakata and Dr. Y. Hoshino of Kanagawa University for assistance in ion implantation. This work was partially supported by a Grant-in-Aid for Scientific Research (No. 24560422) from the Japan Society for the Promotion of Science.

1) J.-P. Colinge, *Silicon-on-Insulator Technology* (Kluwer Academic, Dordrecht, 2004).
2) T. Irisawa, T. Numata, T. Tezuka, K. Usuda, S. Sugiyama, and S. Takagi, IEEE Trans. Electron Devices **55**, 649 (2008).
3) S. Saito, D. Hisamoto, H. Shimizu, H. Hamamura, R. Tsuchiya, Y. Matsui, T. Mine, T. Arai, N. Sugii, K. Torii, S. Kimura, and T. Onai, Jpn. J. Appl. Phys. **45**, L679 (2006).
4) S. Saito, N. Sakuma, Y. Suwa, H. Arimoto, D. Hisamoto, H. Uchiyama, J. Yamamoto, T. Sakamizu, T. Mine, S. Kimura, T. Sugawara, M. Aoki, and T. Onai, IEDM Tech. Dig., 2008, 19.5.
5) T. Mizuno, K. Tobe, Y. Maruyama, and T. Sameshima, Jpn. J. Appl. Phys. **51**, 02BC03 (2012).
6) T. Mizuno, T. Aoki, Y. Nagata, Y. Nakahara, and T. Sameshima, Jpn. J. Appl. Phys. **52**, 04CC13 (2013).
7) T. Mizuno, Y. Nakahara, Y. Nagata, Y. Suzuki, T. Aoki, and T. Sameshima, Jpn. J. Appl. Phys. **53**, 04EC08 (2014).
8) T. Mizuno, Y. Nagata, Y. Suzuki, Y. Nakahara, T. Aoki, and T. Sameshima, Jpn. J. Appl. Phys. **53**, 04EC09 (2014).
9) N. Fukata, T. Oshima, K. Murakami, T. Kizuka, T. Tsurui, and S. Ito, J. Appl. Phys. **100**, 024311 (2006).
10) K. W. Adu, H. R. Gutierrez, and P. C. Eklund, in *Nanosilicon*, ed. V. Kumar (Elsevier, Amsterdam, 2008) Chap. 7.
11) H. Richter, Z. P. Wang, and L. Ley, Solid State Commun. **39**, 625 (1981).
12) I. H. Campbell and P. M. Fauchet, Solid State Commun. **58**, 739 (1986).
13) L. Khriachtchev, M. Rasanen, S. Novikov, O. Kilpela, and J. Sinkkonen, J. Appl. Phys. **86**, 5601 (1999).
14) G. Faraci, S. Gibilisco, P. Russo, and A. R. Pennisi, Phys. Rev. B **73**, 033307 (2006).
15) S. Piscanec, M. Cantoro, A. C. Ferrari, J. A. Zapien, Y. Lifshitz, S. T. Lee, S. Hofmann, and J. Robertson, Phys. Rev. B **68**, 241312(R) (2003).
16) K. Uchida, H. Watanabe, A. Kinoshita, J. Koga, T. Numata, and S. Takagi, IEDM Tech. Dig., 2002, p. 47.
17) K. Uchida, J. Koga, and S. Takagi, J. Appl. Phys. **102**, 074510 (2007).
18) G. Tsutsui, M. Saitoh, and T. Hiramoto, IEEE Trans. Electron Devices **26**, 836 (2005).
19) L. Donetti, F. Gámiz, J. B. Roldán, and A. Godoy, J. Appl. Phys. **100**, 013701 (2006).
20) B. K. Agrawal and S. Agrawal, Appl. Phys. Lett. **77**, 3039 (2000).
21) M. Tabe, M. Kumezawa, and Y. Ishikawa, Jpn. J. Appl. Phys. **40**, L131 (2001).
22) Z. H. Lu and D. Grozea, Appl. Phys. Lett. **80**, 255 (2002).
23) S. S. Iyer and Y.-H. Xie, Science **260**, 40 (1993).
24) S. M. Sze and K. K. Ng, *Physics of Semiconductor Devices* (Wiley, New York, 2007).
25) D. S. Lee and J. G. Fossum, IEEE Trans. Electron Devices **30**, 626 (1983).
26) M. T. Björk, H. Schmid, J. Knoch, H. Riel, and W. Riess, Nat. Nanotechnol. **4**, 103 (2009).
27) T. Mizuno, Y. Nakahara, Y. Nagamine, Y. Suzuki, Y. Nagata, T. Aoki, and T. Sameshima, Ext. Abstr. Solid State Devices and Materials, 2014, p. 854.
28) Web [http://www.soitec.com/en/].
29) A. S. Grove, *Physics and Technology of Semiconductor Devices* (Wiley, New York, 1967).
30) Web [http://www.silvaco.com/].
31) L. Pavesi and R. Turan, *Silicon Nanocrystals* (Wiley-VCH, Weinheim, 2010).
32) M. Diarra, Y.-M. Niquet, C. Delerue, and G. Allan, Phys. Rev. B **75**, 045301 (2007).
33) H. Ikeda and F. Salleh, Appl. Phys. Lett. **96**, 012106 (2010).
34) T. Mizuno, Y. Suzuki, M. Yamanaka, Y. Nagamine, Y. Nakahara, Y. Nagata, T. Aoki, and T. Maeda, Ext. Abstr. Solid State Devices and Materials, 2014, p. 46.